Desalination and Water Treatment
www.deswater.com

doi: 10.5004/dwt.2017.20759

84 (2017) 8–18
July

Surfactant-assisted freeze-drying synthesis of porous graphene for high-performance capacitive deionization

Peng-Hui Wang, Huan Yan, Yifei Xue, Guoqian Lu, Wei Ni, Min Xu, Yi-Ming Yan*

Chemical Engineering and Environment, Beijing Institute of Technology, Beijing, 100081, China, Tel./Fax: +86 10 68918891; email: bityanyiming@163.com (Y.-M. Yan), bitwph@163.com (P.-H. Wang), yanhuan369852147@163.com (H. Yan), 2509490854@qq.com (Y. Xue), 971851443@qq.com (G. Lu), bitniwei@163.com (W. Ni), 653536413@qq.com (M. Xu)

Received 6 July 2016; Accepted 29 March 2017

ABSTRACT

Capacitive deionization (CDI) offers a green and efficient strategy of supplying sustainable clean water. Up to now, high-performance carbon electrode has been substantially pursued for developing advanced CDI technology. In this work, a surfactant-assisted freeze-drying route is reported for the facile synthesis of porous graphene electrode based on the hydrothermal reduction of graphene oxide with ascorbic acid in the presence of sodium dodecyl sulfate (SDS), followed by a freeze-drying treatment. The obtained porous graphene (defined as SRGO) is characterized by scanning electron microscopy, X-ray powder diffraction, elemental distribution analysis, Brunauer-Emmett-Teller adsorption isotherm and Raman spectra. The SRGO exhibits ideal pore size distribution and specific surface area, while the effects of the surfactant on the graphene structural properties are investigated. When used as CDI electrode, the SRGO shows a promising electrosorptive capacity of 5.38 $mg \cdot g^{-1}$, an excellent recyclability (64 min for regeneration), and a remarkable salt removal efficiency of 15.85%. This work opens up a facile and variable route to rationally tailor structural properties of graphene for water treatment applications.

Keywords: Capacitive deionization; Graphene; Sodium dodecyl sulfate; Freeze drying

1. Introduction

Water scarcity has been considered as a severe global challenge due to the growing agriculture and industry [1–6]. In recent years, water treatment technologies, including water purification and desalination, have been tremendously pursued to solve the worldwide water shortage crisis. Specifically, an energy-efficient and environmentally friendly desalination process is urgently demanded. Since 1960s, capacitive deionization (CDI) has attracted numerous research interest because of its advantages, such as easy operation, low maintenance costs and high energy efficiency [6–9]. CDI is an electrochemical based technology to remove salt ions in brackish water by applying an electrical potential across porous electrodes [10]. The principle of CDI is based on electric double-layer capacitor (EDLC) that exploits an external electrostatic field between electrodes to force charged ions to move toward oppositely charged electrode surface. When saturated with ions, the electrodes can be regenerated by releasing the absorbed ions into the following water with a reverse potential. Compared with traditional desalination methods, such as reverse osmosis, electrodialysis and distillation, CDI is a competent desalination strategy that performed at low voltages (<2 V) without apparent environmental impact. However, the efficiency of CDI strongly depends upon the physical properties and internal structure of the electrode materials, because that the charged ions are attracted within the electrical double layer (EDL) formed at the electrode surface [11–15]. Therefore, it is critical to fabricate ideal CDI electrodes, which should own high electrical conductivity, larger surface areas and optimized pore size distribution, to essentially improve the CDI performance.

* Corresponding author.

Several carbon-based materials with high internal surface area and reasonable microporous structure, such as activated carbon, carbon aerogel, carbon nanotube, graphene and their composites, have been typically used for CDI [16]. Among these materials, graphene is considered as a promising candidate for CDI, as it has unique two-dimensional structures, excellent mechanical, electrical and chemical properties, and easily tunable structural feature. Particularly, the theoretical specific surface area of single-layered graphene nanosheet is up to 2,675 $m^2 \cdot g^{-1}$. Assuming that the surface is fully utilized, an intrinsic capacitance and a weight-specific capacitance should be calculated to be 21 $\mu F \cdot cm^{-2}$ and 550 $F \cdot g^{-1}$. This value sets the upper limit of electric double-layer capacitance for carbon-based materials. Unfortunately, during the preparation process, graphene sheets are prone to agglomerate caused by the strong sheet-to-sheet Van der Waals interactions. As a result, this will certainly reduce the specific surface area and deteriorate the internal pore structure of the obtained graphene materials, therefore leading to low EDLC of the electrodes and poor CDI performance [17,18]. To address this problem, many research efforts, such as designing novel structure, developing new synthesis route and introducing guest elements into the graphene, have been devoted in the past years. For example, Wimalasiri and Zou [19] overcome this challenge by inserting one-dimensional carbon nanotubes into graphene layers to prevent the restack of graphene. Garcíaquismondo et al. [20] directly reduced graphite oxide film with laser, getting a graphene film which was mechanically robust, with high electrical conductivity and high specific surface area. Luo et al. [21] transformed the two-dimensional graphene sheet to crumpled paper ball structure to achieve much high specific capacitance. Moreover, Wang et al. [22] used polystyrene microspheres as template to get three-dimensional (3D) graphene structure. With large specific surface area and high conductivity, such carbon electrode has a specific capacitance of 58.4 $F \cdot g^{-1}$ and an electrosorption capacity of 3.9 $mg \cdot g^{-1}$. In our previous work, commercial sponge was utilized as the template to prepare 3D graphene electrode, as well as to achieve high specific surface area and suitable pore size distribution. Sponge can not only serve as support of graphene oxide to prevent the restack of sheets but also control pore size distribution of the porous material [23]. Despite these achievements, developing a green and facile method to fabricate porous graphene materials with suitable structure, high specific surface area and rational pore size distribution is still highly desired for enhancing CDI performance.

Herein, we report for a surfactant-assisted freeze-drying route to synthesize porous graphene material for CDI application. Sodium dodecyl sulfate (SDS) was used as surfactant to get an evenly dispersed graphene oxide (GO) solution by acting as exfoliator and stabilizer. After reduced by ascorbic acid, the GO/SDS mixture was directly freeze dried to obtain 3D structured reduced graphene oxide (SRGO), with reasonable porosity and specific surface area. The obtained SRGO material owns interconnected macroporous structure and exhibits a high specific surface area of 348 $m^2 \cdot g^{-1}$, as well as has a rational pore size distribution. As expected, when used as a CDI electrode, SRGO exhibits a high electrosorption capacity of 5.38 $mg \cdot g^{-1}$ and a fast electrode regeneration rate of 64 min in NaCl solution with an initial concentration of 106 $\mu S \cdot cm^{-1}$. This work opens up a facile and variable route to rationally tailor structural properties of graphene for water treatment applications.

2. Materials and methods

2.1. Materials

Graphite powder (200 mesh 99.9%) was purchased from Alfa Aesar (China) Chemical Co., Ltd. Ethanol (99.7%) was purchased from Beijing Reagent Company, Dongcheng, Beijing. Sulfuric acid (98%), HCl (37%) and H_2O_2 (30%), Ascorbic acid (AR), $KMnO_4$ powders (AR), SDS (AR) were purchased from Beijing Chemical Works, Chaoyang, Beijing. All water used in this work were deionized water. Ethanol (99.7 wt%) was bought from Beijing Reagent Company. Polytetrafluoroethylene (PTFE) suspension solution (16 wt%) was home-prepared.

2.2. Fabrication of surfactant-assisted reduced graphene oxide

The preparation process is shown in Fig. 1. GO was prepared from natural graphite flake by a modified Hummers' method. Then, GO was dispersed in water mixed with SDS through a general ultrasonic treatment to obtain a GO/SDS mixture. After that, ascorbic acid was used to reduce GO by a hydrothermal method after which the mixture was placed in the boiling water bath at 100°C for 1 h. Subsequently, the obtained mixture was thoroughly treated by 24 h dialysis and the obtained materials were submitted for freeze drying. First, the materials were frozen by placing them in a freezer

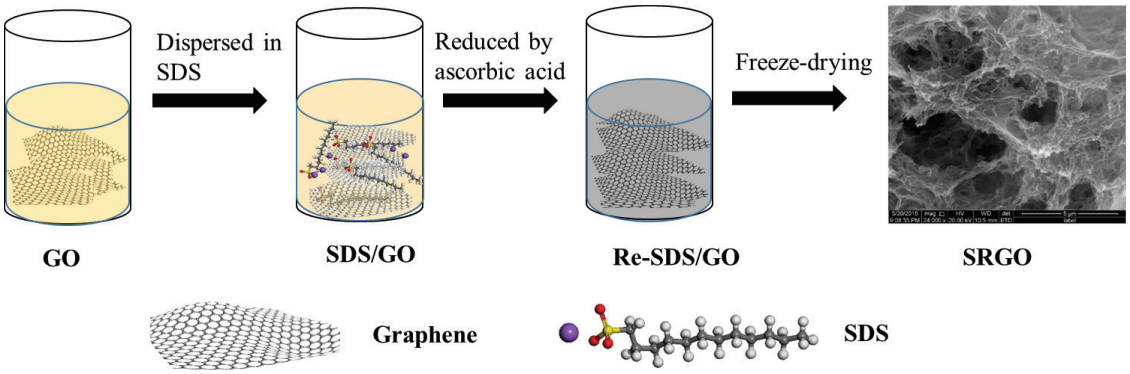

Fig. 1. Schematic representation of the procedure for preparing the SRGO sample.

at a freezing temperature of –10°C for 2 d. After the materials were completely frozen, they were moved to a freeze dryer and dried at a sublimating temperature of –50°C and a pressure of 10 pa for 3 d. The finally obtained solid material was noted as SRGO. For comparison, a sample of reduced graphene oxide was simultaneously prepared following the same procedure except that no surfactant was added (Fig. S1).

Fig. S2 shows the images of the GO solution, SDS/GO solution and SDS/GO solution reduced with ascorbic acid (AA). It is known that GO exhibits amphiphilic feature due to its hydrophilic edges and hydrophobic basal plane [21]. As seen in Fig. S2(a), GO solution gives a transparent solution phase with typical brown color. For comparison, after the addition of SDS, the resulting SDS/GO mixture turns to a yellow color, indicating that SDS should interact with the GO because the surfactant molecule is supposed to intercalate into the GO layers. Furthermore, after reducing by ascorbic acid, the mixture gives a clearly black suspension as shown in Fig. S1(c), indicating the graphene oxide should be successfully reduced to generate graphene layers [24].

2.3. Characterization of carbon electrodes materials

The surface morphology and structure of the as-synthesized samples were examined using scanning electron microscopy (SEM) with energy spectrum analysis (two FEG 250), all of the test results were performed at a beam voltage of 20 kV. The pore size distribution and Brunauer-Emmet-Teller (BET) specific surface area were deduced from the nitrogen physical adsorption measurement data obtained using an Autosorb-IQ2-MP-C system, and the pore size distribution was derived from the adsorption branches of the isotherms using the Barrett-Joyner-Halenda (BJH) model. X-ray diffraction (XRD) spectra were acquired using a tall Rigaku Ultima IV. Raman spectra were recorded with a RM 2000 Raman spectroscopy tester produced by the British Renishaw Gloucestershire, London, which A He-Ne laser (633 nm) was used as the light source for excitation.

2.4. Electrochemical measurements

Electrochemical measurements were performed in three-electrode cell configuration on electrochemical analyzer (CHI660 instruments), which includes a standard Ag/AgCl electrode as reference electrode and a platinum wire as counter electrode. PTFE (Sigma-Aldrich, Shanghai, China; 60 wt% dispersion in water) was added to the mixture of samples and acetylene black (samples/acetylene black/PTFE = 85:10:5 by weight) as a binder. The working electrode was fabricated by casting the mixture on a carbon paper and the electrolyte was 0.5 M NaCl solution. For CDI process, a pair of electrodes with an equal amount of SRGO (or RGO) separated by an insulating spacer was assembled to a water desalination model. The CDI behavior of SRGO and RGO electrodes was carried out in 25 mL NaCl aqueous solution with an initial conductivity of 106 $\mu S \cdot cm^{-1}$ and flow rate of 3 $mL \cdot min^{-1}$. The applied voltage is set as 1.5 V.

3. Results and discussion

3.1. Characterizations of the SRGO sample

To investigate the morphology of the as-prepared SRGO, SEM images were presented in Fig. 1 and the supporting information. As shown in Fig. 2(a), SRGO sample shows a bulky morphology with clearly observed rich and interconnected pores. A high-resolution SEM image, as shown in Fig. 2(b), reveals that the SRGO owns rich macropores, exhibiting well-defined 3D open structure. According to the images, we estimated that the size of the macropores lies at the range of 5–25 μm. Also, it indicates that the walls of the pores are consisted of hybrid graphene layers. It was assumed that the formation of porous structure should be benefited from the freeze-drying treatment, stemming from the cross supporting of the graphene sheets and resulting in a solid and fluffy 3D structure [25]. For comparison, Figs. 2(c) and (d) present the SEM images of RGO. It can be clearly found that RGO sample appears as a bulky morphology with a densely packed surface. No obvious pores can be observed at the surface of RGO. Fig. 2(d) gives the high-magnified image of RGO, revealing that the graphene layers were serious stacked and no pores were observed at the surface. For SRGO and RGO, such a sharp difference of the structure and morphology should be attributed to function of SDS during the preparation. It has been suggested that SDS can act as exfoliator and stabilizer to interact with the GO. The hydrophobic alkyl chain of the SDS is supposed to bind to the aromatic structured GO surface forming surfactant micelle, while the repulsive force between negatively charged part of the SDS and the negatively charged functional groups of GO lead the effective separation of the GO layers. To confirm this assumption, we performed another control experiment by using cetyltrimethyl ammonium bromide (CTAB) as the surfactant. As seen in Fig. S3, the SEM images of CTAB/GO sample shows a disordered aggregation, while a close inspection of the sample indicates that the sample contains thick-layered GO sheets. For comparison, the SDS/GO sample shows large area of GO sheet, and the GO sheet is smooth and thin. The results strongly demonstrate that the positively charged part of the CTAB should accelerate the aggregation of GO sheets. This can be further verified by the phenomenon that the mixing of CTAB with GO solution can apparently lead to the formation of flocculated agglomeration, as shown in the inset of Fig. S3(b). Here, we noted that the SRGO was obtained with a washing treatment by using Milli-Q water and ethanol to remove the SDS after the freeze-drying procedure [26]. The resulted SRGO was investigated by elemental distribution analysis (EDS). As shown in Fig. S4, C element was evenly distributed, while only trace amount of Na was found as the residue of SDS after washing.

For CDI applications, specific surface area and pore size distribution of the carbon material play the key roles in determining the capacitance desalination performance. To characterize the structural and compositional properties of the SRGO, we performed the N_2 adsorption/desorption analysis, as shown in Fig. 3. As seen, the specific surface area of SRGO was calculated to be 348 $m^2 \cdot g^{-1}$, which the value is apparently higher than that of RGO (175 $m^2 \cdot g^{-1}$). Further, acetylene black, which is usually used as conducting additive, was used for comparison, as shown in Fig. S5. As seen, only a specific surface area of 35.8 $m^2 \cdot g^{-1}$ was obtained for acetylene black, which is far lower than that of SRGO. The insets of Figs. 3(a) and (b) show the pore size distribution of the samples, implying a wide distributed range from 3 to 20 nm for SRGO. In contrast, RGO has the pores in sizes mainly less than 5 nm,

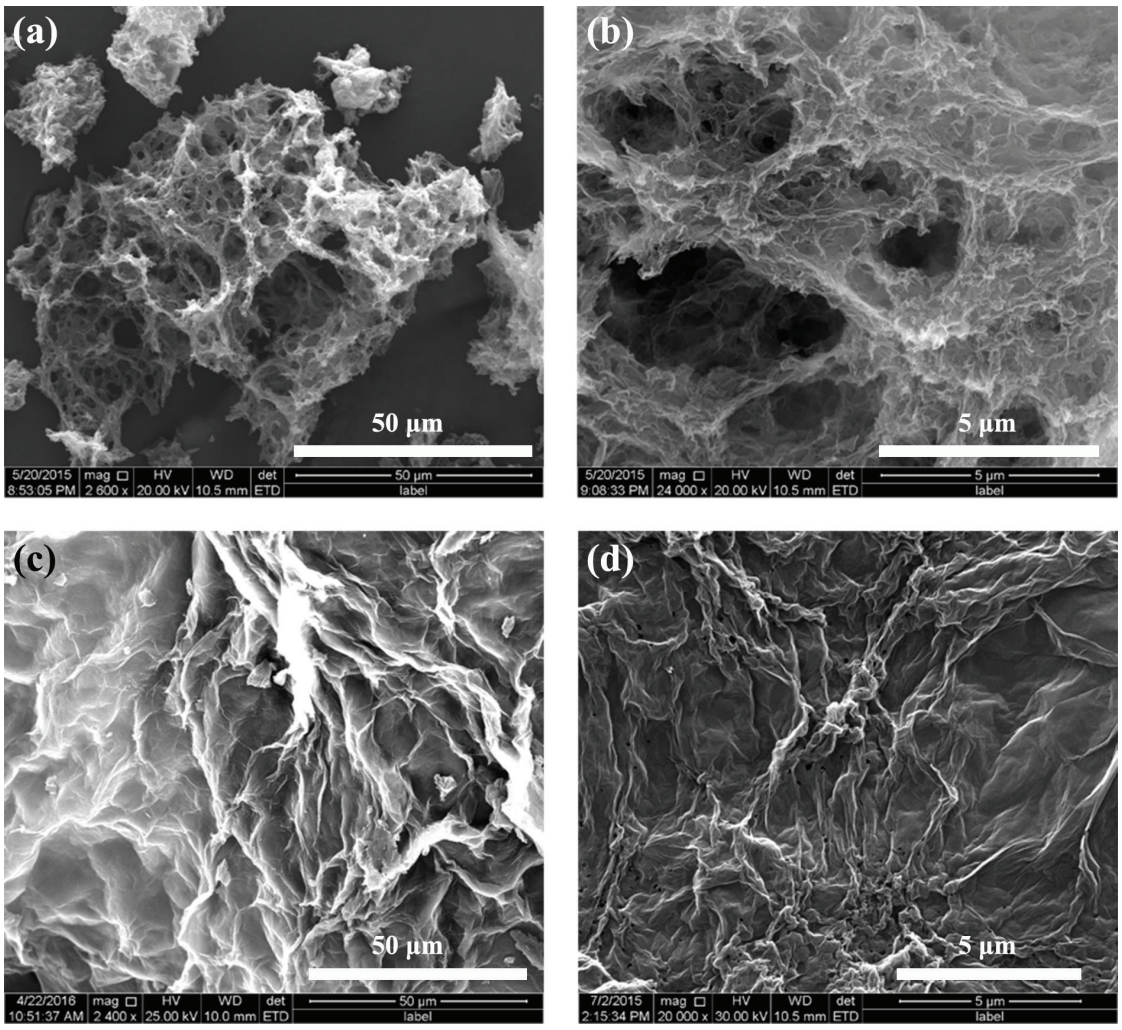

Fig. 2. (a) and (c) SEM images of SRGO and RGO at low magnification, respectively; (b) and (d) SEM images of SRGO and RGO at high magnification.

especially the pores distribute in a size range from 2 to 3 nm. These results strongly demonstrate that the SDS-assisted freeze-drying strategy is an efficient way to obtain SRGO materials with enlarged specific surface area and a wide pore size distribution [27]. It was expected that, for the SRGO, the high BET surface area and reasonable pore distribution should play a critical role in enhancing the adsorption of the salty ions and facilitating the transportation of ions.

We next characterized the SRGO with XRD. The characteristic 2θ peak of the GO powder was at 11° (Fig. S6). For SRGO, as shown in Fig. 2(c), the XRD pattern shows a distinct broad peak at 26°, which is the characteristic peak of graphene [28]. We noted that RGO exhibits similar XRD pattern. The results indicate that the introduction of SDS into the preparation procedure does not affect the XRD patterns of the material. To further understand the physical properties of SRGO and RGO, we conducted Raman spectroscopy. As shown in Fig. 3(d), for carbon materials, the intensity ratio of D and G bands (I_D/I_G) is generally used for evaluating the degree of disorder and average size of sp^2 domains. It is obvious that SRGO and RGO have distinct characteristic peaks at 1,358 and 1,598 cm^{-1}, which are corresponding to the D and G peaks of graphene, respectively. However, a close inspection shows that the intensity ratio of D peak and G peak (I_D/I_G) of SRGO and RGO are 1.287 and 1.184, respectively. The high I_D/I_G ratios for SRGO clearly suggests that there is a decrease in the average size of the in-plane sp^2 domains, which may be attributed to the less layered sheet for SRGO with the assistance of surfactant.

3.2. Electrochemical measurements of the SRGO sample

Due to the well-defined structural properties, the SRGO is supposed to own excellent electrochemical performance. Thus, we performed cyclic voltammetry (CV), galvanostatic charge/discharge (CD). Before testing, the electrode was activated, by immersing in a solution of 0.5 M NaCl for 24 h and then the electrode was washed with deionized water. Fig. 4(a) shows the CV curves of the SRGO measured with various scan rates in the range of 12.5–200 $mV \cdot s^{-1}$ in 0.5 M NaCl aqueous solution. As seen, no redox peaks were observed in the CV curves of SRGO, implying no faradic reaction happens.

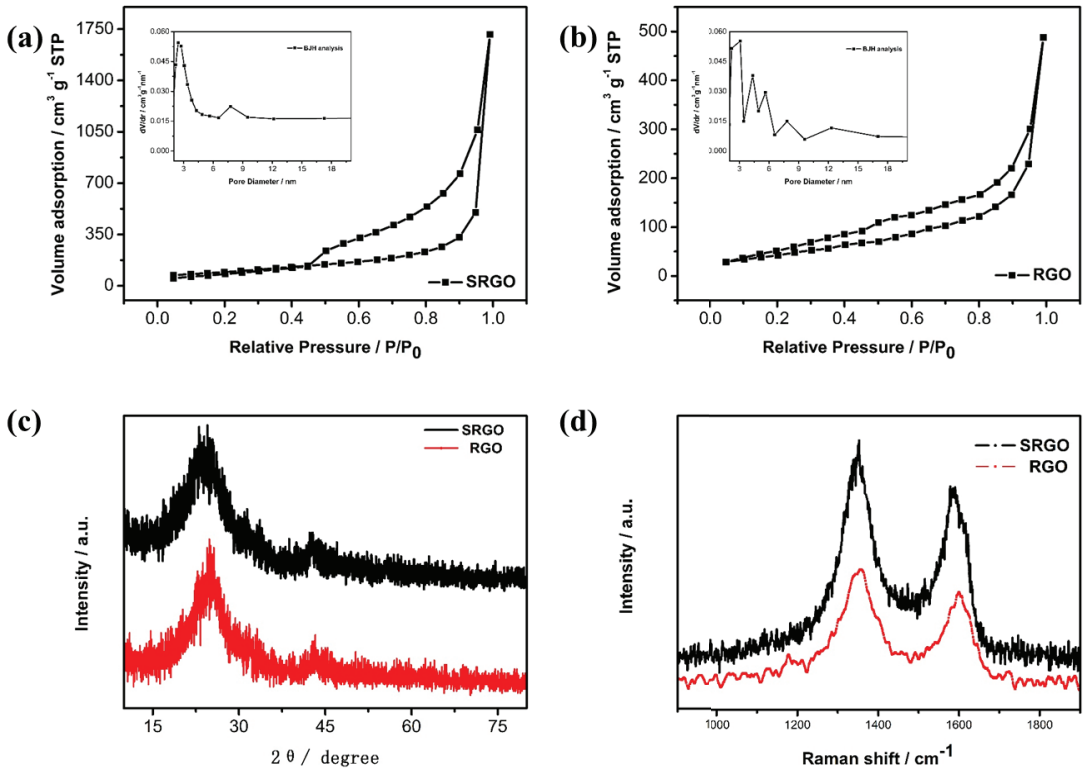

Fig. 3. (a) Nitrogen sorption isotherms of SRGO; the inset shows the BJH pore size distribution plots of SRGO. (b) Nitrogen sorption isotherm of RGO; the inset shows the BJH pore size distribution plots of RGO. (c) XRD patterns of SRGO. (d) Raman spectra of SRGO and RGO.

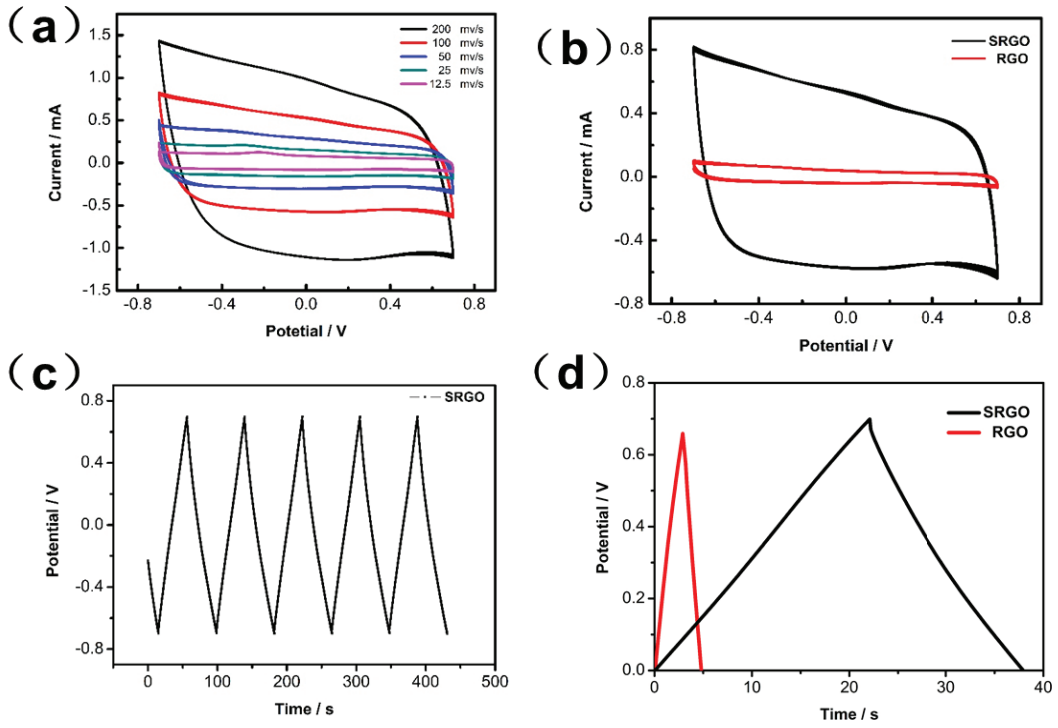

Fig. 4. (a) CV curves of SRGO at different scan rates in 0.5 M NaCl solution; (b) SRGO and RGO at 0.1 V·s^{-1} scan rate in 0.5 M NaCl solution; (c) CD curves of SRGO electrodes in 0.5 M NaCl solution; (d) CD curves of SRGO and RGO electrodes with a current density of 0.1 A·g^{-1}.

Additionally, the CV curves maintain an approximately rectangular shape at each scan rate. It implies that the charge current can reach the plateau quickly, which represents a predominant EDLC characteristic. In contrast, no regular rectangular shape was observed from the CV curves of RGO, especially at high scan rate of 200 mV·s^{-1} (as seen in Fig. S7). It suggests that the RGO electrode exhibits a slower charging kinetic in comparison with SRGO. Fig. 4(b) gives the CV curves of SRGO and RGO electrodes at same scan rate of 100 mV·s^{-1}. Clearly, the SRGO electrode exhibits a remarkably higher charge current in comparison with RGO electrode. As known, the specific capacitances of carbon electrodes could be calculated from the CV results. The specific capacitance (C_s) of electrode can be calculated by using Eq. (1) [29]:

$$C_s = \frac{1}{vw(V_c - V_a)} \int_{V_a}^{V_c} IVdv \quad (1)$$

where v is the scanning rate; w is the quality of the active materials; V_a and V_c represent initial and final potential, respectively; I refers to current and V is voltage [28]. The capacitance of SRGO is calculated to be 241.4 F·g^{-1} at 200 mV·s^{-1} in 0.5 M NaCl solution, higher than that of RGO (26.4 F·g^{-1}). Furthermore, at 25 mV·s^{-1} the capacitance of SRGO and RGO can reach 281.1 and 43.9 F·g^{-1}, respectively. The promising specific capacitance of SRGO should be attributed to its high specific surface area and rational porous structure, which are achieved with the assistance of surfactant. As a consequence, the high capacitance of SRGO indicates that it can form more electrical double layers and adsorb more salty ions, therefore achieving high CDI performance.

We next performed the galvanostatic CD of the two samples. Fig. 4(c) shows the CD curves in a potential window from –0.7 V to 0.7 V at the current density of 0.1 A·g^{-1}. The CD curves of SRGO electrode show classic triangular shapes with symmetric and linear lines, representing typical EDLC behavior and good reversibility. These features are crucial for high efficiency and long-term operation of CDI. The promising CD performance is mainly attributed to the 3D structure of SRGO, which is beneficial for the ionic diffusion of electrolyte into the inner pores. We next performed the galvanostatic CD of SRGO and RGO at same current densities, as shown in Fig. 4(d). Similarly, RGO electrode exhibits a stable CD process, implying typical EDLC behavior and good charge propagation. However, a close comparison shows that SRGO has longer discharge time than RGO does, implying that SRGO possess higher specific capacitance than RGO, which agrees well with the CV results above.

3.3. Capacitive desalination test

Based on the well-characterized structural and electrochemical properties, we expect that SRGO can be used as excellent carbon electrode material for capacitive desalination. To identify this, the CDI behavior of SRGO was examined in 25 mL NaCl aqueous solution with an initial conductivity of 106 μS·cm^{-1}. Two symmetrical SRGO electrodes with the size of 5 cm × 5 cm CDI unit were used in a CDI unit and the distance between two electrodes was 1 mm. The test was carried out at a flow rate of 3 mL·min^{-1}. Fig. 5(a) schematically illustrates the CDI operation, where the system is mainly composed of a peristaltic pump, a DC regulated power supply, an electrochemical cell and a conductivity meter. During the electrosorption process, due to a direct current voltage applied to the CDI cell, ions are rapidly removed from the solution passing through the system until equilibrium is reached. Once the electrodes become saturated with ions, it will be regenerated by releasing the absorbed ions into the flowing water by applying a reversed potential.

Fig. 5(b) displays the variation of conductivity along with the desalination time. The conductivity of salty solution decreased quickly at the beginning, demonstrating a fast electrosorption of salty ions on electrode. And we investigated that the descending rate of conductivity for SRGO electrodes is faster than that of RGO, indicating that salty ions are prone to be easily adsorbed at SRGO electrode. Then, the conductivity of solution decreases slowly until equilibrium is reached with the time going on, which the minimum conductivity of SRGO and RGO are 89.2 and 93.1 μS·cm^{-1}, respectively. And it can be clearly seen that the electrosorption capacity of SRGO

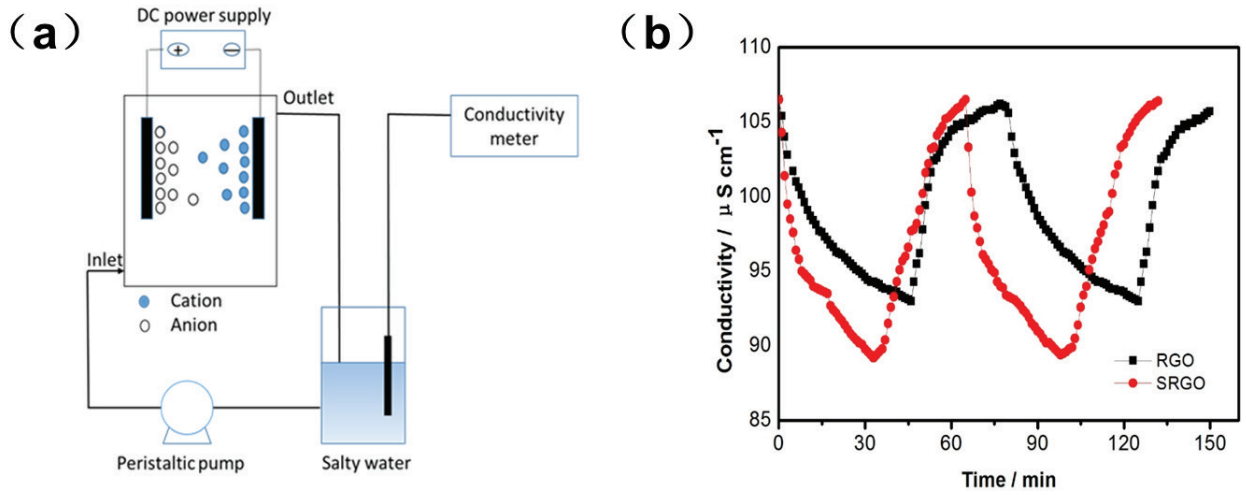

Fig. 5. (a) Schematic representation of the procedure for CDI. (b) Adsorption/desorption profiles of SRGO and RGO electrodes.

is better than RGO, indicating that the introduction of SDS is beneficial to enhance the electrosorption capacity of SRGO. It can be attributed to the favorable pore structure and facilitated ion transport at the electrode–solution interface and faster electron transport within the SRGO electrode. The salt removal efficiencies for SRGO and RGO are 15.9% and 12.2%, respectively. And the salt removal efficiency of the SRGO was improved by 30% compared with that of the initial RGO. This implies that the desalination efficiency of RGO can be improved by the addition of SDS during the synthesis procedure with a freeze-drying treatment, which consequently tune the pore distribution and rationalize the structural properties. Moreover, the electrosorptive capacities are calculated to be 5.38 and 4.13 $mg \cdot g^{-1}$ for SRGO and RGO, respectively. We noted that the electrosorptive capacity of the as-prepared SRGO is higher than most other reported results observed with carbon-based material (see Table S1) [30–41]. Also, Fig. 5(b) presents two CDI cycles for SRGO and RGO electrodes, from which we calculated a rapid regeneration time of SRGO to be 64 min while the value for RGO is 82 min. It demonstrates that the SRGO electrode should possess higher desalination efficiency than RGO. The superior capacitance desalting ability of SRGO should be assigned to its favorable porous structure, large surface area and good electrochemical performance [42]. We expect that this route can be further expanded to be used to fabricate electrodes toward many applications of sensors, electrocatalysis and energy storage.

4. Conclusion

In summary, we have successfully prepared porous graphene electrode material with the assistance of SDS surfactant for capacitive desalination application. A directly freeze-drying treatment was utilized, followed by a reduction with ascorbic acid in a mild and environment-friendly way. We found that the introduction of surfactant helps achieve high specific surface area and rationally tune the pore size distribution of the resulted SRGO materials. The obtained SRGO electrodes have surface area of 348 $m^2 \cdot g^{-1}$ and wide size distribution. For CDI application, the SRGO gives a superior electrosorptive capacity of 5.38 $mg \cdot g^{-1}$ and a fast desorption rate of 64 min. Significantly, the salt removal efficiency of the SRGO is 15.85% which is improved by 30% compared with that of the initial RGO. This work may open up a facile and variable route to rationally tailor structural properties of graphene for water treatment or energy storage applications.

Acknowledgments

Financial supports from the National Natural Science Foundation of China (Grant nos. 21175012, 21575016), and the Central Organization Department Young Excellent Personnel Program are gratefully acknowledged.

References

[1] G. Xin, O. Ayokunle, L. James, L. Kunlei, Enhanced salt removal in an inverted capacitive deionization cell using amine modified microporous carbon cathodes, Environ. Sci. Technol., 49 (2015) 10920–10926.
[2] Y. Oren, Capacitive deionization (cdi) for desalination and water treatment — past, present and future (a review), Desalination, 228 (2008) 10–29.
[3] S. Porada, L. Borchardt, M. Oschatz, M. Bryjak, J.S. Atchison, K.J. Keesman, S. Kaskel, P.M. Biesheuvel, V. Presser, Direct prediction of the desalination performance of porous carbon electrodes for capacitive deionization, Energy Environ. Sci., 6 (2013) 3700–3712.
[4] Y. Wang, A.G. Eldeen, P. Li, B.H. Oh, Z. Guo, M.M. Khin, Y.S. Vikhe, J. Wang, R.G. Hu, R.M. Boom, K.A. Kline, D.L. Becker, H.W. Duan, M.B. Chan-Park, High-performance capacitive deionization disinfection of water with graphene oxide-graft-quaternized chitosan nanohybrid electrode coating, ACS Nano, 9 (2015) 10142–10157.
[5] G.Q. Lu, G.W. Wang, P.H. Wang, Z.Y. Yang, H. Yan, W. Ni, L. Zhang, Y.M. Yan, Y. Yu, Enhanced capacitive deionization performance with carbon electrodes prepared with a modified evaporation casting method, Desalination, 2016, 386, 32–38.
[6] J.H. Yeo, J.H. Choi, Enhancement of nitrate removal from a solution of mixed nitrate, chloride and sulfate ions using a nitrate-selective carbon electrode, Desalination, 320 (2013) 10–16.
[7] Y. Liu, X. Xingtao, W. Miao, L. Ting, S. Zhuo, P. Likun, Nitrogen-doped carbon nanorods with excellent capacitive deionization ability, J. Mater. Chem. A, 3 (2015) 17304–17311.
[8] X. Xu, Y. Liu, T. Lu, Z. Sun, D.H.C. Chua, L. Pan, Rational design and fabrication of graphene/carbon nanotubes hybrid sponge for high-performance capacitive deionization, J. Mater. Chem. A, 3 (2015) 13418–13425.
[9] J.H. Lee, W.S. Bae, J.H. Choi. Electrode reactions and adsorption/desorption performance related to the applied potential in a capacitive deionization process, Desalination, 258 (2010) 159–163.
[10] M.E. Suss, T.F. Baumann, W.L. Bourcier, C.M. Spadaccini, K.A. Rose, J.G. Santiago, M. Stadermann, Capacitive desalination with flow-through electrodes, Energy Environ. Sci., 5 (2012) 9511–9519.
[11] Y. Wimalasiri, L. Zou, Carbon nanotube/graphene composite for enhanced capacitive deionization performance, Carbon, 59 (2013) 464–471.
[12] K. Laxman, M.T.Z. Myint, M.A. Abri, P. Sathe, S. Dobretsov, J. Dutta, Desalination and disinfection of inland brackish ground water in a capacitive deionization cell using nanoporous activated carbon cloth electrodes, Desalination, 362 (2015) 126–132.
[13] L. Mustafa, P.J. King, K. Umar, D. Sukanta, J.N. Coleman, High-concentration, surfactant-stabilized graphene dispersions, ACS Nano, 4 (2010) 3155–3162.
[14] M. Lotya, Y. Hernandez, P.J. King, R.J. Smith, V. Nicolosi, L.S. Karlsson, F.M. Blighe, S. De, Z. Wang, I.T. McGovern, G.S. Duesberg, J.N. Coleman, Liquid phase production of graphene by exfoliation of graphite in surfactant/water solutions, J. Am. Chem. Soc., 131 (2009) 3611–3620.
[15] P. Liang, L. Yuan, X. Yang, S. Zhou, X. Huang, Coupling ion-exchangers with inexpensive activated carbon fiber electrodes to enhance the performance of capacitive deionization cells for domestic wastewater desalination, Water Res., 47 (2013) 2523–2530.
[16] A.G. El-Deen, N.A.M. Barakat, H.Y. Kim, Graphene wrapped MnO_2-nanostructures as effective and stable electrode materials for capacitive deionization desalination technology, Desalination, 344 (2014) 289–298.
[17] F. Duan, X. Du, Y. Li, H. Cao, Y. Zhang, Desalination stability of capacitive deionization using ordered mesoporous carbon: effect of oxygen-containing surface groups and pore properties, Desalination, 376 (2015) 17–24.
[18] H. Yin, S. Zhao, J. Wan, H. Tang, L. Chang, L.C. He, H.J. Zhao, Y. Gao, Z.Y. Tang, Three-dimensional graphene/metal oxide nanoparticle hybrids for high-performance capacitive deionization of saline water, Adv. Mater., 25 (2013) 6270–6276.
[19] Y. Wimalasiri, L. Zou, Carbon nanotube/graphene composite for enhanced capacitive deionization performance, Carbon, 59 (2013) 464–471.
[20] E. Garcíaquismondo, C. Santos, J. Lado, J. Palma, M.A. Anderson, Optimizing the energy efficiency of capacitive deionization reactors working under real-world conditions, Environ. Sci. Technol., 47 (2013) 11866–11872.

[21] J. Luo, H.D. Jang, J. Huang, Effect of sheet morphology on the scalability of graphene-based ultracapacitors, ACS Nano, 7 (2013) 1464–1471.
[22] H. Wang, D.S. Zhang, T.T. Yan, X.R. Wen, L.Y. Shi, Q.D. Zhang, Three-dimensional macroporous graphene architectures as high performance electrodes for capacitive deionization, J. Mater. Chem. A, 1 (2013) 11778–11789.
[23] Z.Y. Yang, L. Jin, G.Q. Lu, Q. Xiao, Y.X. Zhang, L. Jing, X. Zhang, Y.M. Yan, K.N. Sun, Sponge-templated preparation of high surface area graphene with ultrahigh capacitive deionization performance, Adv. Funct. Mater., 24 (2014) 3917–3925.
[24] H. Wang, L. Shi, T. Yan, J. Zhang, Q. Zhong, D. Zhang, Design of graphene-coated hollow mesoporous carbon spheres as high performance electrodes for capacitive deionization, J. Phys. Chem. A, 2 (2014) 4739–4750.
[25] Y.J. Kim, J. Hur, W. Bae, J.H. Choi, Desalination of brackish water containing oil compound by capacitive deionization process, Desalination, 253 (2010) 119–123.
[26] C.J. Shih, G.L.C. Paulus, Q.H. Wang, J. Zhong, D. Blankschtein, M.S. Strano, Understanding surfactant/graphene interactions using a graphene field effect transistor: relating molecular structure to hysteresis and carrier mobility, Langmuir, 28 (2012) 8579–8586.
[27] Z. Wang, B.J. Dou, L. Zheng, G.N Zhang, Z.H. Liu, Z.P. Hao, Effective desalination by capacitive deionization with functional graphene nano composite as novel electrode material, Desalination, 299 (2012) 96–102.
[28] M.E. Suss, S. Porad, X. Sun, P.M. Biesheuvel, J. Yoon, V. Presser, Water desalination via capacitive deionization: what is it and what can we expect from it? Energy Environ. Sci., 8 (2015) 2296–2319.
[29] Y. Cai, Y. Wang, X. Han, L. Zhang, S. Xu, J. Wang, Optimization on electrode assemblies based on ion-doped polypyrrole/carbon nanotube composite in capacitive deionization process, J. Electroanal. Chem., 768 (2016) 72–80.
[30] Q. Liu, Y. Wang, Y. Zhang, S. Xu, J. Wang, Effect of dopants on the adsorbing performance of polypyrrole/graphite electrodes for capacitive deionization process, Synth. Met., 162 (2012) 655–661.
[31] L. Zou, L. Li, H. Song, G. Morris, Using mesoporous carbon electrodes for brackish water desalination, Water Res., 42 (2008) 2340–2348.
[32] H.B. Li, L.K. Pan, Y.P. Zhang, L. Zou, C.Q. Sun, Y.K. Zhan, Z. Sun, Kinetics and thermodynamics study for electrosorption of NaCl onto carbon nanotubes and carbon nanofibers electrodes, Chem. Phys. Lett., 485 (2010) 161–166.
[33] C. Farmer, D.V. Fix, G.V. Mack, R.W. Pekala, J.F. Poco, Capacitive deionization of NH_4 ClO_4 solutions with carbon aerogel electrodes, J. Electrochem. Soc., 143 (1996) 159–169.
[34] R. Zhao, P.M. Biesheuvel, H. Miedema, H. Bruning, A. van der Wal, Charge efficiency: a functional tool to probe the double-layer structure inside of porous electrodes and application in the modeling of capacitive deionization, J. Phys. Chem. Lett., 1 (2010) 205–210.
[35] D.S. Zhang, T.T. Yan, L.Y. Shi, Z. Peng, X.R. We, J.P. Zhang, Enhanced capacitive deionization performance of graphene/carbon nanotube composites, J. Mater. Chem., 22 (2012) 14696–14704.
[36] D.S. Zhang, X.R. Wen, L.Y. Shi, T.T. Yan, J.P. Zhang, Enhanced capacitive deionization of graphene/mesoporous carbon composites, Nanoscale, 4 (2012) 5440–5446.
[37] W. Gang, D. Qiang, L. Zheng, P. Chao, Y. Chang, J. Qiu, Hierarchical activated carbon nanofiber webs with tuned structure fabricated by electrospinning for capacitive deionization, J. Mater. Chem., 22 (2012) 21819–21823.
[38] H. Li, L. Pan, C. Nie, Y. Liu, Z. Sun, Reduced graphene oxide and activated carbon composites for capacitive deionization, J. Mater. Chem., 22 (2012) 15556–15561.
[39] L. Wang, M. Wang, Z.H. Huang, T. Cui, X. Gui, F. Kang, K.L. Wang, D.H. Wu, Capacitive deionization of NaCl solutions using carbon nanotube sponge electrodes, J. Mater. Chem., 21 (2011) 18295–18299.
[40] X.R. Wen, D.S. Zhang, L.Y. Shi, T.T. Yan, H. Wang, J.P. Zhang, Graphene prepared via a novel pyridine–thermal strategy for capacitive deionization, J. Mater. Chem., 22 (2012) 23835–23844.
[41] H. Wang, D.S. Zhang, T.T. Yan, X.R. Wen, J.P. Zhang, L.Y. Shi, Q.D. Zhong, Three-dimensional macroporous graphene architectures as high performance electrodes for capacitive deionization, J. Mater. Chem. A, 1 (2013) 11778–11789.
[42] G.X. Wang, J. Yang, J. Park, X.L. Gou, B. Wang, H. Liu, J.N. Yao, Facile synthesis and characterization of graphene nanosheets, J. Phys. Chem. C, 112 (2008) 8192–8195.

Supporting information

Preparation of GO

GO was prepared according to the method reported in our previous work [23]. In brief, graphite powder was put into a solution of concentrated nitric acid and sulphuric acid (152 in volume) and kept at 80°C for 5 h. The mixture was cooled to room temperature, diluted with deionized (DI) water and left overnight. Then, the reaction vessel was immersed in an ice bath, and potassium permanganate was added slowly. Successively, the mixture was stirred and left for 2 h. Then, after the dilution with DI water, 30% H_2O_2 was added into the mixture, and the color of mixture changed into brilliant yellow along with bubbling. Finally, the mixture was filtered and washed with HCl aqueous solution (1,510 in volume), DI and ethanol, respectively. Finally, the obtained GO was dried in vacuum oven at 60°C for 24 h.

The electrosorption capacity (q_e) of per active material cell can be calculated using Eq. (1) while the deionization efficiency (η_d) can be calculated using Eq. (2).

$$q_e = \frac{V_{\text{olume}}(C_{\text{eff}} - C_0)}{w} \tag{1}$$

$$\eta_d(\%) = \left(1 - \frac{C_{\text{eff}}}{C_0}\right) \times 100 \tag{2}$$

where w is the quality of the active materials; V_{olume} is the volume of NaCl solution and C_0 is the initial concentration; C_{eff} is the lowest concentration at adsorption equilibrium.

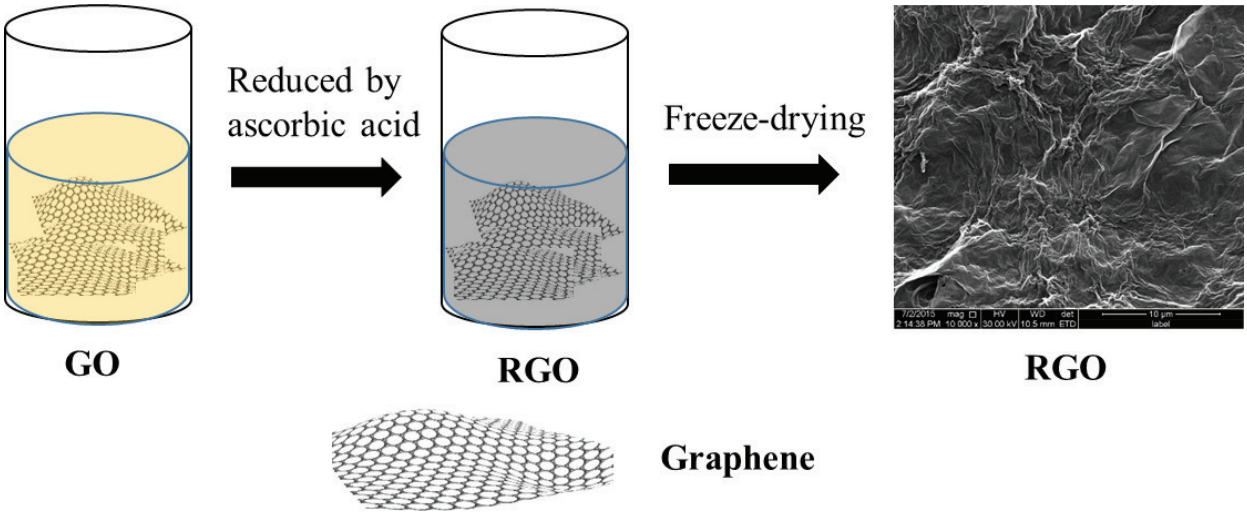

Fig. S1. Schematic representation of the procedure for preparing the RGO samples.

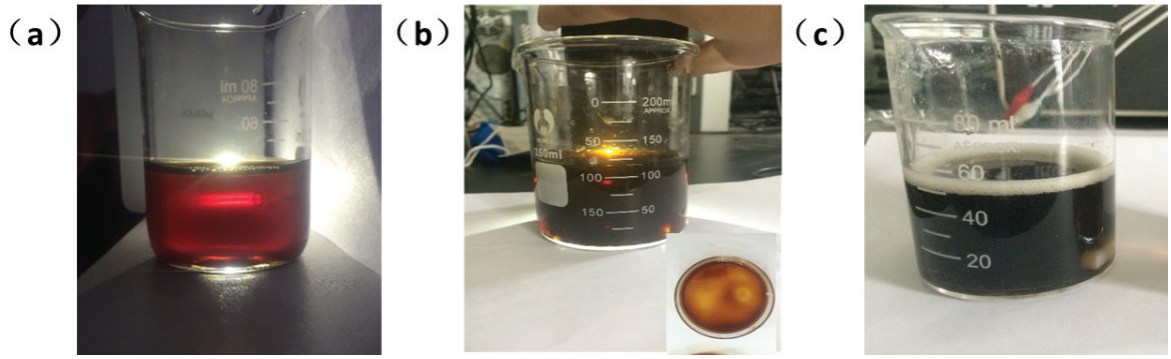

Fig. S2. Photo images of (a) GO solution, (b) SDS/RGO mixture solution before reducing by AA, and (c) SDS/RGO solution after reduction.

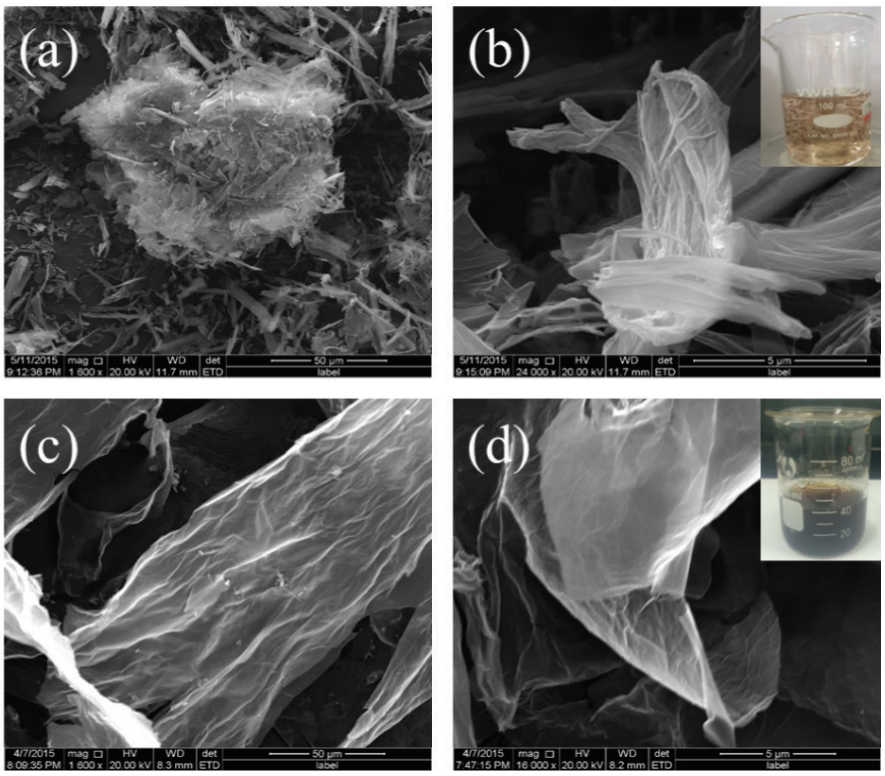

Fig. S3. SEM images of CTAB/GO at low (a) and high (b) resolution, and SDS/GO at low (a) and high (b) resolution.

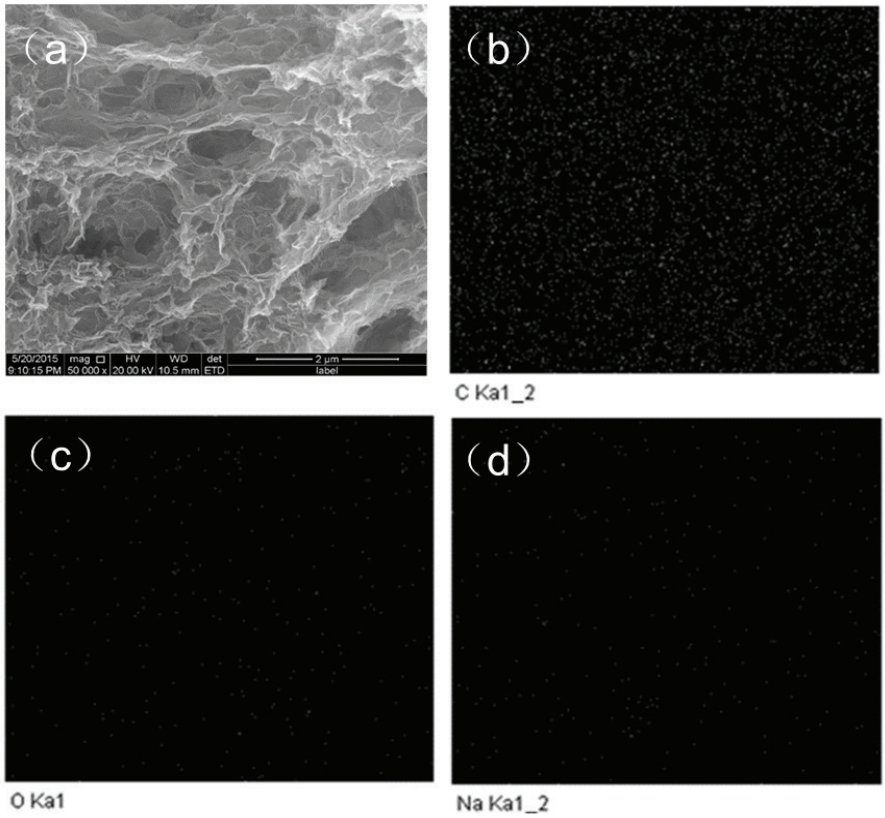

Fig. S4. Elemental distribution analysis (EDS) of the SRGO.

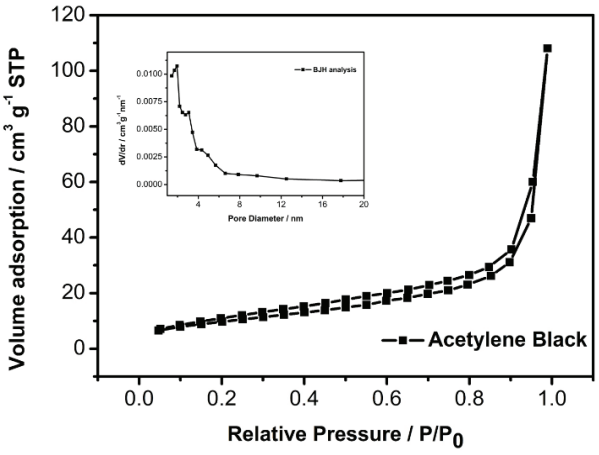

Fig. S5. Nitrogen sorption isotherms of acetylene black; the inset shows the pore size distribution.

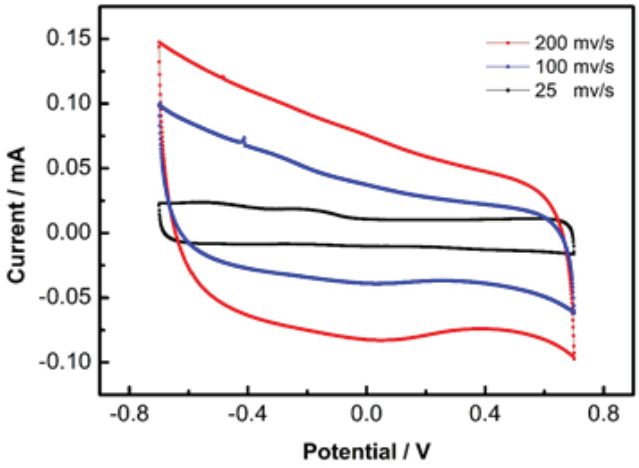

Fig. S7. CV curves of RGO at different scan rates in 0.5 M NaCl solution.

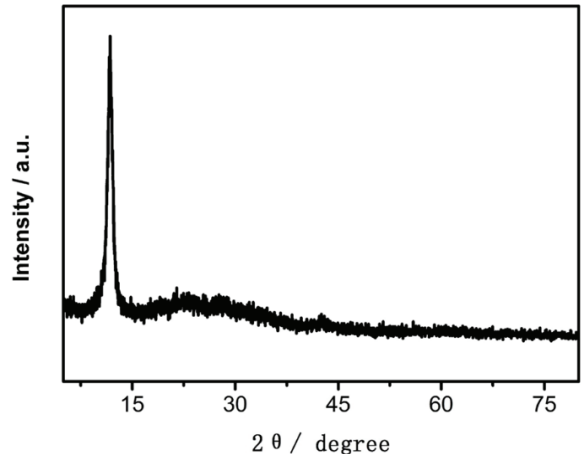

Fig. S6. XRD patterns of GO.

Table S1
Comparison of electrosorption capacity among different electrode materials

Electrode (units)	Electrosorption capacity (both electrodes) (mg g^{-1})	Specific surface area ($m^2 g^{-1}$)	Initial solution concentration (μS cm^{-1})	Applied voltage (V)	Reference
STGS	4.95	305	106 μS cm^{-1}	1.5	[23]
RGO-RF	1.0023	406.4	55 μS cm^{-1}	1.5	[30]
OMCs	0.68	968	51 μS cm^{-1}	1.2	[31]
CNTs/CNFs	3.32	211	100 μS cm^{-1}	1.2	[32]
CAs	3.33	400–1,100	100 μS cm^{-1}	1.2	[33]
ACs	11.7	1,130	5–20 mM	1.2	[34]
GR/CNT	1.41	365.1–479.5	57 μS cm^{-1}	1.0	[35]
GE/MC	0.731	624.7–677.3	89.5 μS cm^{-1}	2	[36]
ACF/CB	1.99	917	197 μS cm^{-1}	1.6	[37]
GAC	2.94	779	50 μS cm^{-1}	1.2	[38]
A7 ACF	8.9	670	1 mM	1.5	[39]
3DHPC	2.16	1,036.8	65 μS cm^{-1}	2	[40]
3DMGA	1.97–5.39	339	108.6 μS cm^{-1}	1.2–2	[41]
EPD-CNTs	2.33	82	100 μS cm^{-1}	1.2	[32]
SRGO	5.38	348	106 μS cm^{-1}	1.5	This work